


Cite this: *RSC Adv.*, 2022, 12, 13220

# Solid oxide fuel cell with a spin-coated yttria stabilized zirconia/gadolinia doped ceria bi-layer electrolyte

Jingyu Li,<sup>ab</sup> Lijun Fan,<sup>ab</sup> Nianjun Hou,<sup>ab</sup> Yicheng Zhao<sup>ID</sup>\*<sup>ab</sup> and Yongdan Li<sup>ID</sup><sup>abc</sup>

A thin yttria stabilized zirconia (YSZ)/gadolinia doped ceria (GDC) bi-layer membrane is fabricated through the slurry spin coating technique and used as an electrolyte of a solid oxide fuel cell with  $\text{La}_{0.6}\text{Sr}_{0.4}\text{Co}_{0.2}\text{Fe}_{0.8}\text{O}_{3-\delta}$  as the cathode. The viscosity of the YSZ slurry is controlled by adding ethanol in the terpineol solvent, which shows a negligible effect on the thickness but a remarkable influence on the porosity of the YSZ film. The thickness of the YSZ layer increases with the YSZ content in the slurry. The YSZ films are pre-sintered at various temperatures, and the one sintered at 1200 °C has a moderate interaction with the GDC slurry, forming a 10  $\mu\text{m}$ -thick YSZ/GDC bilayer with a low porosity and a low ohmic resistance. The corresponding single cell shows a maximum power density of 1480  $\text{mW cm}^{-2}$  at 750 °C.

Received 29th March 2022

Accepted 23rd April 2022

DOI: 10.1039/d2ra02035a

rsc.li/rsc-advances

## 1. Introduction

The solid oxide fuel cell (SOFC) with high energy conversion efficiency, fuel flexibility and low emissions is widely recognized as a promising power generation technology.<sup>1,2</sup> The practical application of the SOFC is mainly hindered by its high operating temperature, which limits the selection of component materials, increases the cost and reduces the durability. The low oxygen ionic conductivity of the traditional yttria-stabilized zirconia (YSZ) electrolyte, about 0.13  $\text{S cm}^{-1}$  at 1000 °C,<sup>3</sup> is one of the main reasons for the high operating temperature, and electrolyte materials with a higher ionic conductivity, such as doped ceria,<sup>4,5</sup> doped  $\text{LaGaO}_3$ ,<sup>6</sup>  $\text{Er}_{0.4}\text{Bi}_{1.6}\text{O}_{3-\delta}$ ,<sup>7</sup>  $\text{Sr}_{0.55}\text{Na}_{0.45}\text{SiO}_{2.775}$ ,<sup>8,9</sup>  $\text{Na}_{0.5}\text{Bi}_{0.49}\text{Ti}_{0.98}\text{Mg}_{0.02}\text{O}_{3-\delta}$  (ref. 10) and proton-conducting perovskite oxides,<sup>11,12</sup> have been extensively explored over the past decades. Unfortunately, those substitutes usually suffer from high electronic conductivity or low stability under operating conditions. So far, YSZ is still the most commonly used electrolyte material in commercial SOFC systems.

Reducing the thickness of YSZ electrolyte layer is one of the major strategies for lowering the working temperature and boosting the performance of SOFC. For SOFC operated below

750 °C, the thickness of YSZ layer should be generally less than 15  $\mu\text{m}$ .<sup>13</sup> In recent years, many deposition methods, such as pulsed laser deposition,<sup>14</sup> atomic layer deposition,<sup>15</sup> chemical vapor deposition<sup>16</sup> and sputtering,<sup>17</sup> have been used to fabricate thin YSZ films with high quality. However, the high cost of those processes limits their large-scale application.

As a fast and cost-effective technique, slurry spin coating has been widely used to prepare gas-tight oxide electrolyte films.<sup>18–20</sup> Wang *et al.*<sup>21</sup> fabricated a 10  $\mu\text{m}$ -thick YSZ membrane on a NiO-YSZ anode support with slurry spin coating, and the maximum power density ( $P_{\text{max}}$ ) of the single cell reaches 2  $\text{W cm}^{-2}$  at 800 °C. Chen *et al.*<sup>22</sup> coated a 10  $\mu\text{m}$ -thick anode functional layer (AFL) and a 5  $\mu\text{m}$ -thick YSZ electrolyte membrane successively on a NiO-YSZ anode support, and the  $P_{\text{max}}$  of the cell is 0.6  $\text{W cm}^{-2}$  at 800 °C. Many parameters of the spin coating process, such as the viscosity and solid content of the slurry, the spinning speed and duration, number of coating cycles and the property of AFL, have important effect on the thickness and porosity of the electrolyte layer. A higher spinning speed generally results in a thinner and denser membrane.<sup>23,24</sup> Kim *et al.*<sup>25</sup> found that rising the binder content in the slurry leads to the increase of thickness and porosity of the electrolyte layer. Buchkremer and co-workers<sup>26,27</sup> optimized the size of YSZ nanoparticles in the slurry. Nevertheless, the relationships among the component and the viscosity of the slurry and the morphology of the electrolyte membrane have not been revealed clearly. Moreover, in order to avoid the interaction between YSZ and traditional perovskite cathode materials such as  $\text{La}_{0.6}\text{Sr}_{0.4}\text{Co}_{0.2}\text{Fe}_{0.8}\text{O}_{3-\delta}$  (LSCF), a thin doped ceria interlayer is usually required, which, however, will react with YSZ during the sintering process and form an insulating Ce–Zr solid solution phase.<sup>28–30</sup>

<sup>a</sup>State Key Laboratory of Chemical Engineering (Tianjin University), Tianjin Key Laboratory of Applied Catalysis Science and Technology, School of Chemical Engineering and Technology, Tianjin University, Tianjin, 300072, China. E-mail: zhaoyicheng@tju.edu.cn

<sup>b</sup>Collaborative Innovation Center of Chemical Science and Engineering (Tianjin), Tianjin, 300072, China

<sup>c</sup>Department of Chemical and Metallurgical Engineering, Aalto University, Kemistintie 1, FI-00076 Aalto, Finland



In this work,  $\text{YSZ/Ce}_{0.9}\text{Gd}_{0.1}\text{O}_{2-\delta}$  (GDC) bi-layer electrolyte is prepared with the slurry spin coating method. The effects of the solvent composition and the YSZ content on the viscosity of the slurry and the morphology of the YSZ membrane are discussed. The YSZ film is pre-sintered at various temperatures before the coating of the GDC layer. The interaction between YSZ and GDC phases and its influence on the cell performance are investigated.

## 2. Experimental

### 2.1. Material preparation

GDC powder was prepared through a coprecipitation process with oxalic acid as the precipitant.<sup>31</sup> LSCF powder was synthesized *via* a glycine–nitrate combustion approach.<sup>32</sup> The LSCF and GDC powders were mixed at a weight ratio of 1 : 1 through ball-milling to form the LSCF–GDC composite cathode.

### 2.2. Single cell fabrication

NiO–YSZ composite anode support layer was prepared through a cold-press approach. NiO (Shanghai Aladdin Bio-Chem Technology Co., Ltd, 99%), YSZ (Shanghai Naiou Nano technology Co., Ltd, 99.9%, particle size: 50 nm) and starch at a weight ratio of 56 : 44 : 9 were ball-milled in ethanol for 12 h. After drying, the composite powder was pressed at 300 MPa into a pellet with a diameter of 15 mm, which was sintered in air at 1100 °C for 3 h. The thickness of the obtained anode support layer is about 650  $\mu\text{m}$ .

NiO–YSZ anode functional layer (AFL) was prepared *via* a spin-coating method. NiO and YSZ powders were mixed at a weight ratio of 56 : 44 through ball-milling. Terpeneol (Shanghai Meryer Chemical Technology Co., Ltd, 99%), ethyl cellulose (EC, Tianjin Yuanli Chemical Technology Co., Ltd, AR) and ethanol (Shanghai Titan Scientific Co., Ltd, AR) were mixed at a weight ratio of 62 : 3 : 35 to form an organic solvent. The NiO–YSZ composite powder was mixed with the solvent at a weight ratio of 1 : 5 to form the AFL slurry, which was spin-coated on the anode support at 1000 rpm for 30 s and subsequently at 10 000 rpm for 60 s. Then the organics were removed at 420 °C in air for 1 h. The spin-coating procedure was repeated three times.

YSZ electrolyte layer was also fabricated by the spin-coating method. 1 wt% EC was dissolved in 99 wt% terpeneol, which was then mixed with ethanol to form the solvent. The concentration of ethanol in the solvent was in the range of 25–55 wt%. Subsequently, YSZ powder was added in the solvent, followed by ball-milling for 12 h to form the YSZ electrolyte slurry. The content of YSZ in the slurry was in the range of 25–40 wt%. The spin-coating procedure of the YSZ layer was similar to that of the AFL, which was repeated twice. YSZ/GDC bi-layer electrolyte was also prepared. After the deposition of one YSZ layer, the pellet was pre-sintered at 1000–1300 °C for 4 h, and a GDC layer was spin-coated on the YSZ layer. For the GDC slurry, the concentration of ethanol in the solvent and the content of GDC in the slurry were both 25 wt%. After the spin-coating process of the electrolyte layers, the pellets were sintered in air at 1400 °C for 4 h to form half cells.

The LSCF–GDC composite cathode powder was mixed with a binder (V006, Heraeus Ltd) to form the cathode slurry. The slurry was screen-printed on the electrolyte layer and sintered at 950 °C for 3 h. The geometrical area of the cathode was 0.28  $\text{cm}^2$ . Ag paste was coated on the electrodes as the current collector.

### 2.3. Characterization

The crystal structures of the GDC and LSCF powders were investigated at room temperature using an X-ray diffractometer (XRD, D8 Focus, Bruker Cor., Germany) with  $\text{Cu-K}\alpha$  radiation, 40 kV and 200 mA, at a scanning rate of  $8^\circ \text{min}^{-1}$ . The morphology of the components of the single cell was observed with a scanning electron microscope (SEM, Apreo S LoVac, FEI, USA). The viscosity of the slurry for spin-coating was measured with a viscosimeter (NDJ-79, Shanghai Ni Run Intelligent Technology Co., Ltd, China).

### 2.4. Electrochemical property

The current–voltage ( $I$ – $V$ ) curve of the single cell was measured with an electrochemical workstation (VersaSTAT 3, Ametek, USA) with  $\text{H}_2$  (30  $\text{mL min}^{-1}$ , STP) and oxygen (50  $\text{mL min}^{-1}$ , STP) as the fuel and the oxidant, respectively. The electrochemical impedance spectroscopy (EIS) of the cell was recorded in a frequency range of 1 MHz to 0.1 Hz with an amplitude of 10 mV.

## 3. Results and discussion

### 3.1. Characterization of synthesized powders and AFL

The XRD patterns of GDC and LSCF powders are presented in Fig. 1a. GDC shows a cubic fluorite structure (JCPDS #75-0162) and LSCF exhibits a perovskite structure (JCPDS #49-0284), which are consistent with the results of previous works without any impure phases.<sup>33–36</sup> The cross-sectional SEM image of the anode support and anode functional layers sintered at 1400 °C is shown in Fig. 1b. Large pores with an average diameter of about 20  $\mu\text{m}$  distribute unevenly in the anode support layer. The thickness of

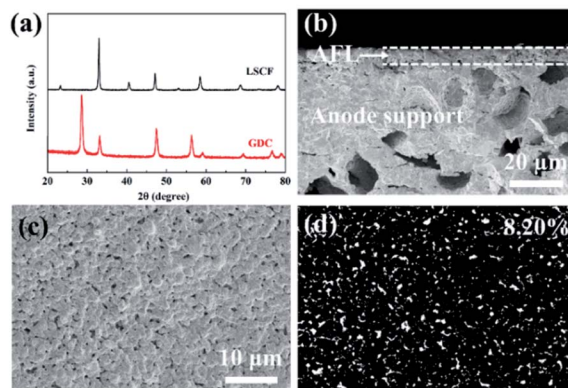


Fig. 1 (a) XRD patterns of GDC and LSCF powders; (b) cross-sectional SEM image of the anode support and anode functional layers sintered at 1400 °C; (c and d) surface SEM image of the AFL. The pits on the AFL are detected and measured with ImageJ software.

the AFL is about 6  $\mu\text{m}$ , and dense adhesion is achieved between the anode support layer and AFL. The surface porosity of the AFL is 8.20%, and the average pore size is 200–300 nm.

### 3.2. Single cells with YSZ electrolyte layer

**3.2.1. Effects of the solvent.** The viscosities of the solvents with various ethanol contents are listed in Table 1. The viscosity of pure terpineol is 24.0 mPa s, which drops sharply to 7.0 mPa s when 25 wt% ethanol is added in the solvent, and then decreases gradually with the further addition of ethanol. The viscosity of the ethanol–terpineol mixed solvent increases remarkably with the addition of EC, and a higher viscosity is observed after adding 50 wt% YSZ to form the electrolyte slurry.

Fig. 2 shows the morphology of the electrolyte layers with various ethanol contents in the solvent. With 50 wt% YSZ in the electrolyte slurry, the thickness of the two-cycle YSZ layer after sintering is about 25  $\mu\text{m}$ , which is almost unaffected by the content of ethanol. On the contrary, the ethanol content in the solvent of the electrolyte slurry shows a remarkable influence on the porosity of the electrolyte layer. The YSZ layer with 25 wt%

ethanol in the solvent exhibits a high surface porosity of 5.16%, which is probably due to the relatively high viscosity (24.0 mPa s) of the electrolyte slurry, resulting in an uneven distribution of the YSZ powder.<sup>28</sup> The YSZ slurry with 35 wt% ethanol in the solvent shows a moderate viscosity (14.5 mPa s), and thus the corresponding electrolyte layer has the lowest surface porosity of 1.24%. The further addition of ethanol in the solvent leads to an increase of the surface porosity to 3.5–4.3%. The YSZ slurry with a low viscosity (8–11.5 mPa s) may partly permeate into the AFL during the spin-coating and the drying processes (Fig. 2c and d), rising the porosity of the electrolyte layer.<sup>37</sup>

The current–voltage ( $I$ – $V$ ) and current–power ( $I$ – $P$ ) characteristics of the single cells at 750  $^{\circ}\text{C}$  are presented in Fig. 3. The open circuit voltage (OCV) of the 25 wt%-ethanol cell is only 0.83 V due to the high porosity of the electrolyte layer, and the  $P_{\text{max}}$  is 454  $\text{mW cm}^{-2}$ . The 35 wt%-ethanol cell with the most compact electrolyte film shows the highest OCV and  $P_{\text{max}}$  of 1.07 V and 1136  $\text{mW cm}^{-2}$ , respectively. The OCV and  $P_{\text{max}}$  of the cell both drop with more ethanol in the solvent of the electrolyte slurry due to the porosity increase of the YSZ membrane.

**Table 1** Viscosities of the solvents with various ethanol contents and the corresponding electrolyte slurries. The YSZ content in the electrolyte slurry is 50 wt%

Ethanol/(ethanol + terpineol)	Viscosity (mPa s)		
	Ethanol–terpineol solvent	Ethanol–terpineol–EC solvent	Ethanol–terpineol–EC–YSZ slurry
0 wt%	24.0	—	—
25 wt%	7.0	18.0	24.0
35 wt%	5.0	10.5	14.5
45 wt%	3.5	7.0	11.5
55 wt%	2.8	4.5	8.0

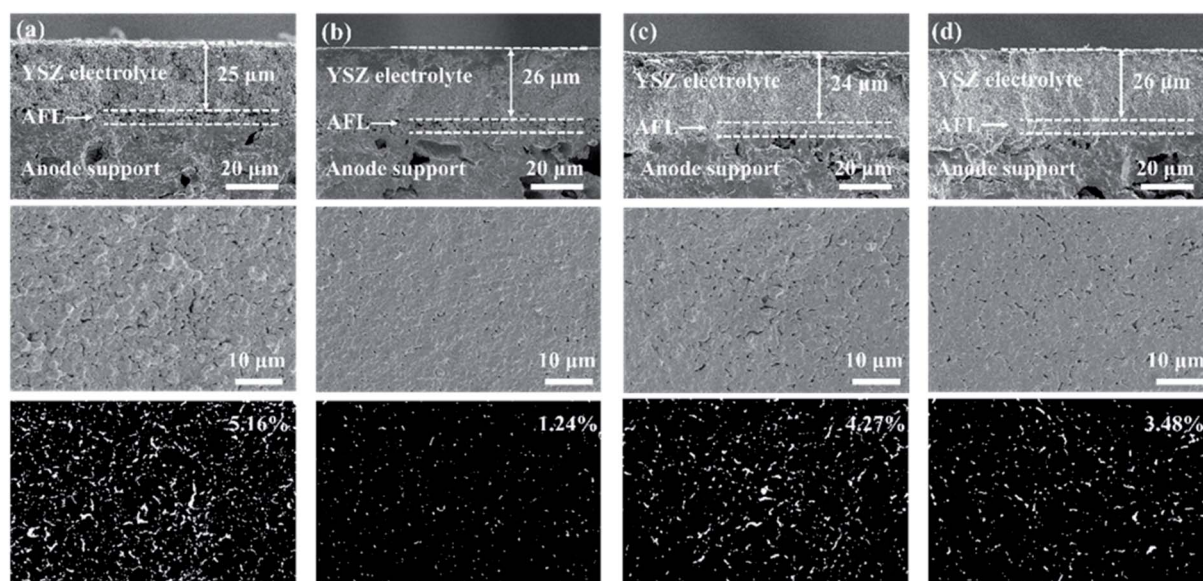


**Fig. 2** Cross-sectional and surface SEM images of the two-cycle YSZ layers with (a) 25 wt%, (b) 35 wt%, (c) 45 wt% and (d) 55 wt% ethanol in the solvent. The YSZ content in the electrolyte slurry is 50 wt%. The pits on the surface of the electrolyte layers are detected and measured with ImageJ software.





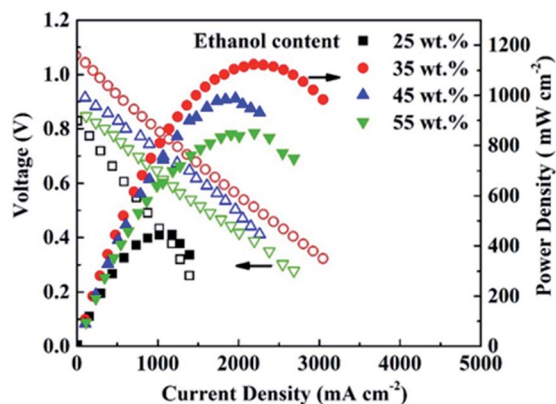


Fig. 3  $I$ - $V$  and  $I$ - $P$  curves of the single cells at 750 °C with various ethanol contents in the solvent.

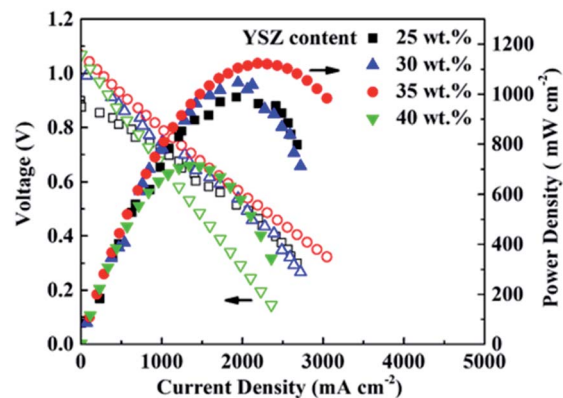


Fig. 5  $I$ - $V$  and  $I$ - $P$  curves of the single cells at 750 °C with various YSZ contents in the electrolyte slurry.

**3.2.2. Effects of the YSZ content.** The viscosity of the ethanol-terpineol-EC solvent with 35 wt% ethanol is 10.5 mPa s (Table 1), which increases with the addition of YSZ powder. The viscosities of the slurries containing 25 wt%, 30 wt%, 35 wt% and 40 wt% YSZ are 12.5, 13.5, 14.5 and 19.5 mPa s, respectively. The morphology of the two-cycle YSZ layers with different YSZ contents in the slurry is shown in Fig. 4. The slurry with a higher YSZ content makes a thicker electrolyte layer, which is consistent with the results of previous works.<sup>21,38</sup> The surface porosity of the electrolyte layer with 25 wt% YSZ in the slurry is 5.93%. The increase of the YSZ content in the slurry to 30 and 35 wt% results in the decrease of the surface porosity to 3.08% and 1.24%, respectively. However, when the amount of YSZ in the slurry reaches 40 wt%, the surface porosity of the electrolyte layer increases to 4.78% mainly due to the difference in thermal expansion coefficients between the AFL and the YSZ layers.<sup>38,39</sup> The

relatively high viscosity of the 40 wt% YSZ slurry is another probable reason for the high porosity of the electrolyte layer.

The  $I$ - $V$  and  $I$ - $P$  curves of the single cells at 750 °C are presented in Fig. 5. The OCV of the 25 wt%-YSZ cell with the highest porosity of the electrolyte layer is 0.91 V, and the corresponding  $P_{\max}$  is 998 mW cm<sup>-2</sup>. The OCVs of the cells with higher YSZ contents are in the range of 1.00–1.07 V. The  $P_{\max}$  of 30 wt%-YSZ and 35 wt%-YSZ cells are 1066 and 1136 mW cm<sup>-2</sup>, respectively. When the amount of YSZ in the slurry reaches 40 wt%, the  $P_{\max}$  of the cell decreases to 725 mW cm<sup>-2</sup> mainly due to the high ohmic resistance of the thick electrolyte layer.

### 3.3. Single cells with YSZ/GDC bi-layer electrolyte

The surface SEM images of the one-cycle YSZ layers sintered at various temperatures are shown in Fig. 6. The average size of

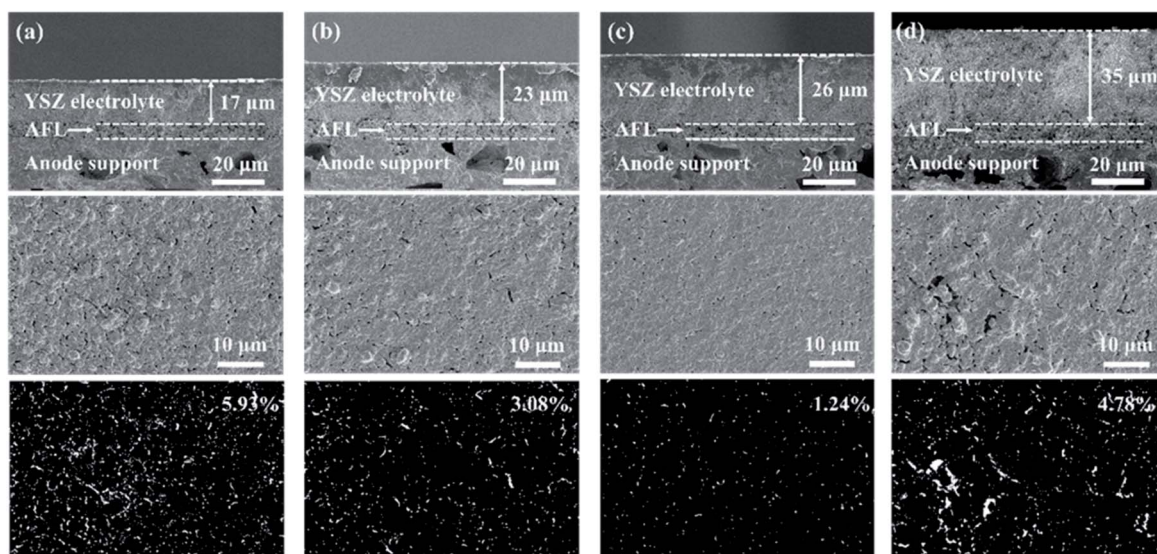


Fig. 4 Cross-sectional and surface SEM images of the two-cycle YSZ layers with (a) 25 wt%, (b) 30 wt%, (c) 35 wt% and (d) 40 wt% YSZ in the electrolyte slurry. The ethanol content in the solvent is 35 wt%. The pits on the surface of the electrolyte layers are detected and measured with ImageJ software.

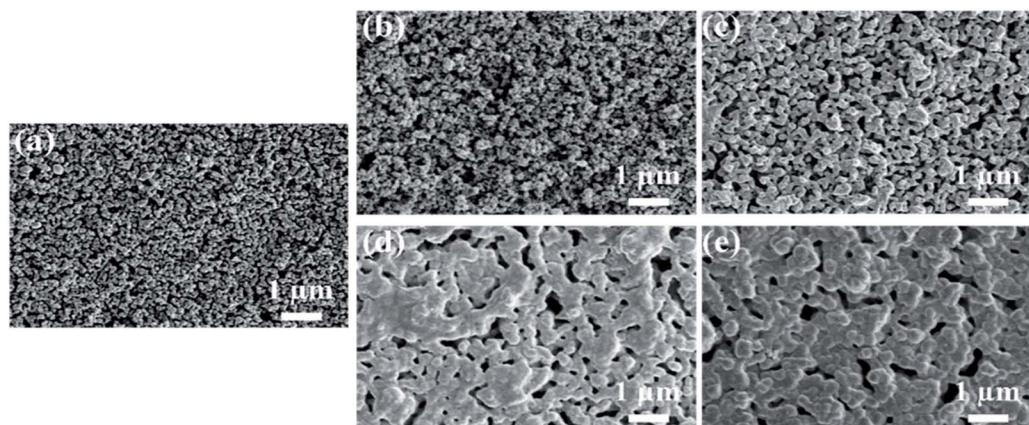


Fig. 6 Surface SEM images of the one-cycle YSZ layers sintered at (a) 420 °C, (b) 1000 °C, (c) 1100 °C, (d) 1200 °C and (e) 1300 °C.

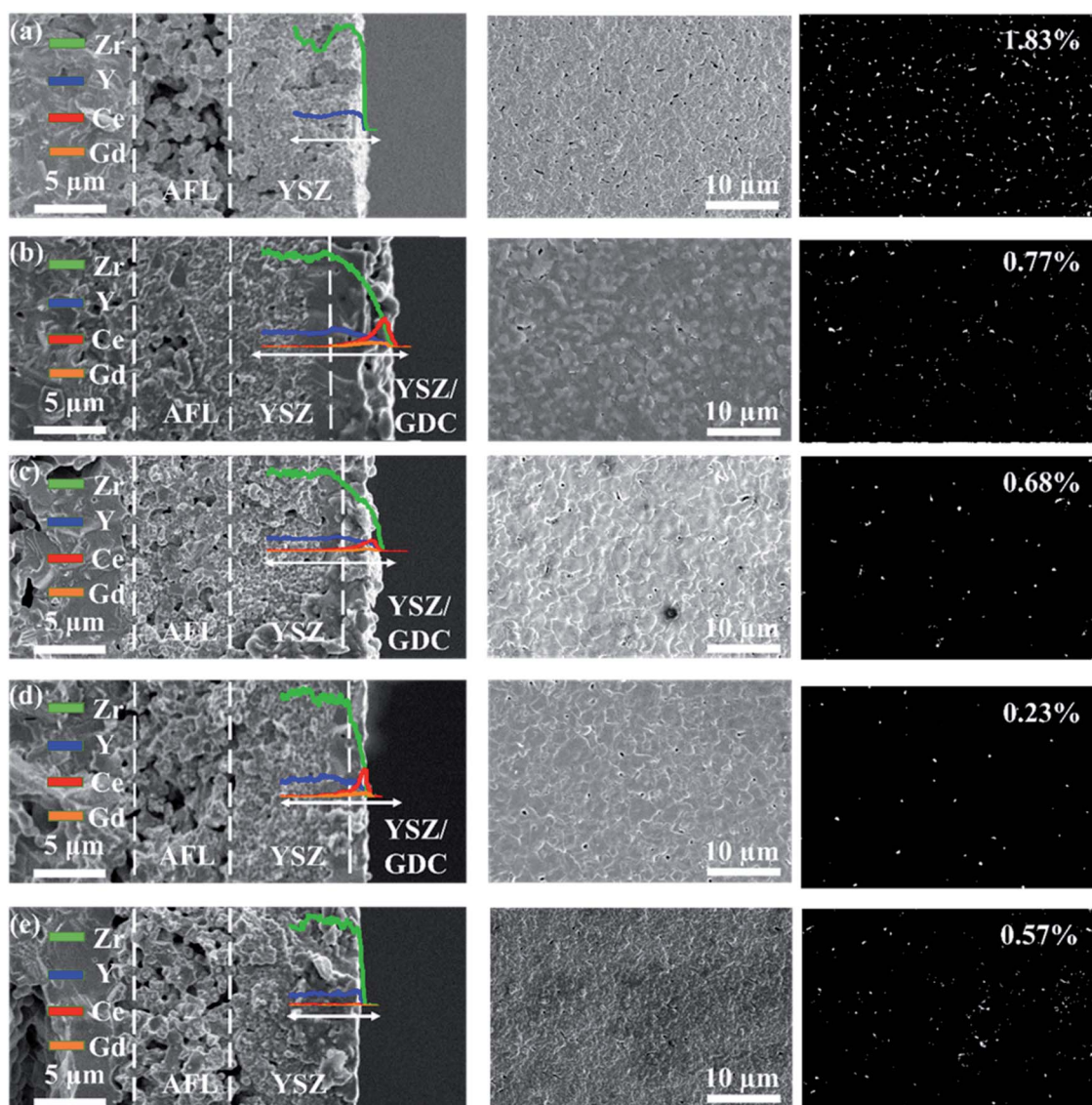


Fig. 7 Cross-sectional SEM images with the line-scanning results and surface SEM images of (a) one-cycle YSZ layer, and YSZ/GDC bilayers in which the YSZ layer was pre-sintered at (b) 1000 °C, (c) 1100 °C, (d) 1200 °C and (e) 1300 °C. The pits on the surface of the electrolyte layers are detected and measured with ImageJ software.





YSZ particles sintered at 420 °C is about 50 nm, which increases to about 100 and 200 nm when the temperature rises to 1000 and 1100 °C, respectively. The grain growth of YSZ is more obvious when the temperature is higher than 1200 °C.

The cross-sectional and surface SEM images of the one-cycle YSZ layer sintered at 1400 °C are shown in Fig. 7a. The YSZ layer shows a thickness of about 9  $\mu\text{m}$  and a surface porosity of 1.83%. The infiltration of GDC into the YSZ layer is found in the YSZ/GDC bi-layer electrolytes in which the YSZ layer was pre-sintered at 1000 °C (Fig. 7b), 1100 °C (Fig. 7c) and 1200 °C (Fig. 7d), resulting in a YSZ/GDC composite layer on the surface. The YSZ layer pre-sintered at a lower temperature has a smaller grain size and a larger porosity (Fig. 6), leading to a deeper infiltration of GDC. Meanwhile, the surface roughness of the YSZ layer is reduced with the increase of the pre-sintering temperature, resulting in a weak interaction between the YSZ layer and the GDC slurry, and thus less GDC slurry remains on the YSZ layer after spin-coating. The thicknesses of the composite layers on YSZ-1000, YSZ-1100 and YSZ-1200 are 3.8, 2.5 and 1.4  $\mu\text{m}$ , respectively. The YSZ/GDC composite layers are much denser than the YSZ layer, and the composite electrolyte layer on YSZ-1200 has the lowest surface porosity of 0.23%. Only a small amount of GDC is found on the surface of YSZ-1300 without the formation of a noticeable YSZ/GDC composite layer (Fig. 7e) probably due to the large grain size and the low porosity of YSZ-1300, which weakens the interaction between the YSZ layer and the GDC slurry during the spin-coating process. Nonetheless, the surface porosity of the YSZ layer is

reduced to 0.57%, indicating the infiltration of a small amount of GDC into the YSZ-1300 layer.

The EIS results of the single cells with YSZ/GDC electrolyte layers at 750 °C are presented in Fig. 8a. The high-frequency intercept of the curve on the real axis reflects the ohmic resistance ( $R_o$ ) of the cell, and the arc corresponds to the polarization resistance ( $R_p$ ). The YSZ-1000 cell shows the largest  $R_o$  due to its thickest electrolyte layer. Moreover, the insulating Ce–Zr solid solution probably formed between the YSZ and GDC phases leads to the increase of both  $R_o$  and  $R_p$ . As a result, the YSZ-1000 cell shows the lowest  $P_{\text{max}}$  of 460  $\text{mW cm}^{-2}$  at 750 °C (Fig. 8b). The interaction between the YSZ and GDC phases is weakened with the increase of the pre-sintering temperature of the YSZ membrane, resulting in the decrease of  $R_o$  and  $R_p$ . The YSZ-1200 cell has the lowest  $R_o$  and  $R_p$  and consequently the highest  $P_{\text{max}}$  of 1480  $\text{mW cm}^{-2}$  at 750 °C. However,  $R_o$  increases when the pre-sintering temperature of the YSZ layer rises to 1300 °C probably due to the absence of the GDC interlayer, leading to the interaction between the YSZ electrolyte and the LSCF cathode. The  $P_{\text{max}}$  of the cell decreases with the drop of the operating temperature. The YSZ-1200 cell exhibits  $P_{\text{max}}$  of 872, 472 and 215  $\text{mW cm}^{-2}$  at 700, 650 and 600 °C, respectively (Fig. 8c). The short-term durability of the YSZ-1200 cell was tested at 700 °C with an output current density of 500  $\text{mA cm}^{-2}$  (Fig. 8d). The output voltage decreases gradually from 0.79 V to 0.70 V during the first 7 h, and decreases slowly to 0.63 V in the next 33 h, indicating a promising stability of the single cell with a YSZ/GDC bi-layer electrolyte.

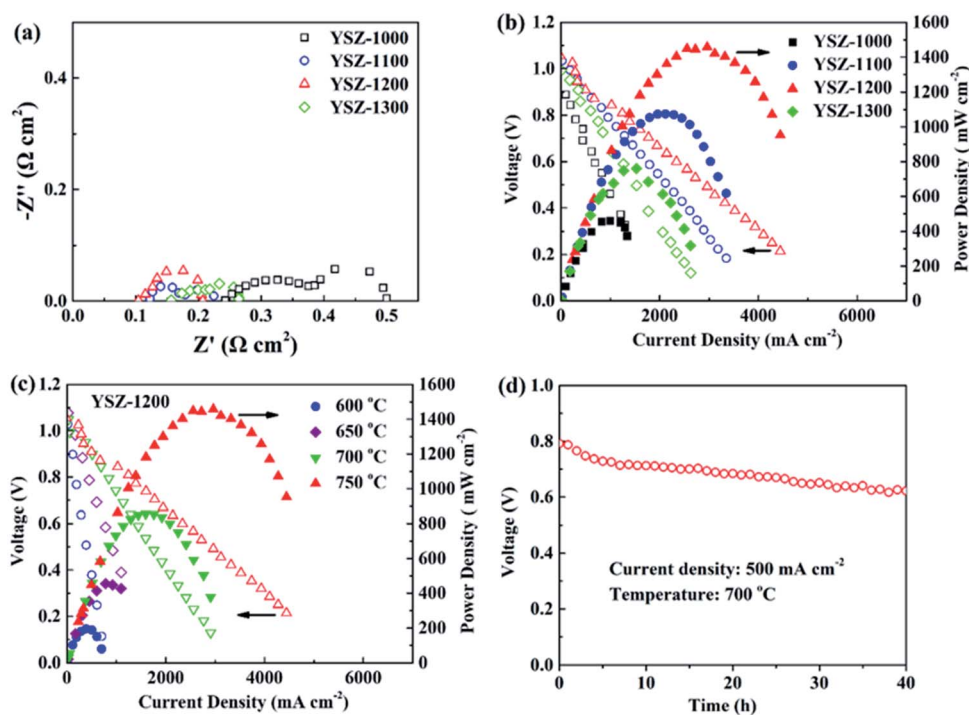


Fig. 8 (a) EIS results and (b)  $I$ - $V$  and  $I$ - $P$  curves of the single cells with YSZ/GDC bilayers at 750 °C in which the YSZ layers were pre-sintered at various temperatures; (c)  $I$ - $V$  and  $I$ - $P$  curves of the YSZ-1200 cell at various temperatures; (d) durability of the YSZ-1200 cell at 700 °C under a constant output current density of 500  $\text{mA cm}^{-2}$ .



## 4. Conclusion

In this work, YSZ and YSZ/GDC electrolyte layers are fabricated with the slurry spin coating method. A lower ethanol content in the terpeneol solvent and a higher YSZ content result in a higher viscosity of the YSZ slurry. The thickness of the YSZ film is influenced negligibly by the viscosity but increases with the YSZ content of the slurry. The most compact YSZ layer is produced using a slurry with 35 wt% ethanol in the solvent and 35 wt% YSZ in the slurry. The YSZ layer is pre-sintered at various temperatures, and the interaction between the YSZ membrane and the GDC slurry is weakened with the rise of the pre-sintering temperature. A strong interaction leads to the formation of insulating Ce–Zr solid solution, while a weak interaction results in insufficient adherence of GDC to the YSZ membrane. The YSZ-1200 cell shows the highest  $P_{\max}$  of 1480 mW cm<sup>-2</sup> at 750 °C. The cell also exhibits a promising stability.

## Conflicts of interest

There are no conflicts to declare.

## Acknowledgements

The financial support from National Natural Science Foundation of China under contract number 22075205 and the support of Tianjin Municipal Science and Technology Commission under contract number 19JCYBJC21700 are gratefully acknowledged. The work has been also supported by the Program of Introducing Talents to the University Disciplines under file number B06006, and the Program for Changjiang Scholars and Innovative Research Teams in Universities under file number IRT 0641.

## References

- 1 P. Boldrin, E. Ruiz-Trejo, J. Mermelstein, J. M. B. Menendez, T. R. Reina and N. P. Brandon, *Chem. Rev.*, 2016, **116**, 13633–13684.
- 2 P. A. Connor, X. L. Yue, C. D. Savaniu, R. Price, G. Triantafyllou, M. Cassidy, G. Kerherve, D. J. Payne, R. C. Maher, L. F. Cohen, R. I. Tomov, B. A. Glowacki, R. V. Kumar and J. T. S. Irvine, *Adv. Energy Mater.*, 2018, **8**, 1800120.
- 3 N. Mahato, A. Banerjee, A. Gupta, S. Omar and K. Balani, *Prog. Mater. Sci.*, 2015, **72**, 141–337.
- 4 S. Buyukkilic, S. Kim and A. Navrotsky, *Angew. Chem., Int. Ed.*, 2014, **53**, 9517–9521.
- 5 D. Kalaev, T. Defferriere, C. Nicollet, T. Kadosh and H. L. Tuller, *Adv. Funct. Mater.*, 2020, **30**, 1907402.
- 6 T. Ishihara, H. Matsuda and Y. Takita, *J. Am. Chem. Soc.*, 1994, **116**, 3801–3803.
- 7 E. D. Wachsman and K. T. Lee, *Science*, 2011, **334**, 935–939.
- 8 P. Singh and J. B. Goodenough, *J. Am. Chem. Soc.*, 2013, **135**, 10149–10154.
- 9 T. Wei, P. Singh, Y. H. Gong, J. B. Goodenough, Y. H. Huang and K. Huang, *Energy Environ. Sci.*, 2014, **7**, 1680–1684.
- 10 M. Li, M. J. Pietrowski, R. A. De Souza, H. R. Zhang, I. M. Reaney, S. N. Cook, J. A. Kilner and D. C. Sinclair, *Nat. Mater.*, 2014, **13**, 31–35.
- 11 C. C. Duan, J. H. Tong, M. Shang, S. Nikodemski, M. Sanders, S. Ricote, A. Almansoori and R. O'Hayre, *Science*, 2015, **349**, 1321–1326.
- 12 Y. Zhou, X. F. Guan, H. Zhou, K. Ramadoss, S. Adam, H. J. Liu, S. Lee, J. Shi, M. Tsuchiya, D. D. Fong and S. Ramanathan, *Nature*, 2016, **534**, 231–234.
- 13 B. C. H. Steele and A. Heinzl, *Nature*, 2001, **414**, 345–352.
- 14 J. H. Park, S. M. Han, B. K. Kim, J. H. Lee, K. J. Yoon, H. Kim, H. I. Ji and J. W. Son, *Electrochim. Acta*, 2019, **296**, 1055–1063.
- 15 B. C. Yang, S. Kye, D. Go, S. Oh, H. J. Kim, J. W. Shin, G. Y. Cho and J. An, *Ceram. Int.*, 2021, **47**, 11372–11378.
- 16 D. Y. Jang, M. Kim, J. W. Kim, K. Bae, J. W. Son, M. V. F. Schlupp and J. H. Shim, *J. Electrochem. Soc.*, 2017, **164**, F484–F490.
- 17 S. Ryu, W. Yu, I. Chang, T. Park, G. Y. Cho and S. W. Cha, *Ceram. Int.*, 2020, **46**, 12648–12655.
- 18 C. Viazzi, V. Rouessac, P. Lenormand, A. Julbe, F. Ansart and C. Guizard, *J. Power Sources*, 2011, **196**, 2987–2993.
- 19 A. Mineshige, A. Saito, M. Kobayashi, H. Hayakawa, M. Momai, T. Yazawa, H. Yoshioka, M. Sakao, R. Mori, Y. Takayama, Y. Kagoshima and J. Matsui, *J. Power Sources*, 2020, **475**, 228543.
- 20 K. R. Lee, C. J. Tseng, S. C. Jang, J. C. Lin, K. W. Wang, J. K. Chang, T. C. Chen and S. W. Lee, *Int. J. Hydrogen Energy*, 2019, **44**, 23784–23792.
- 21 J. M. Wang, Z. Lu, K. F. Chen, X. Q. Huang, N. Ai, J. Y. Hu, Y. H. Zhang and W. H. Su, *J. Power Sources*, 2007, **164**, 17–23.
- 22 S. N. Chen, D. G. Gu, Y. F. Zheng, H. Chen and L. C. Guo, *J. Mater. Sci.*, 2020, **55**, 88–98.
- 23 E. H. Kang, H. R. Choi, J. S. Park, K. H. Kim, D. H. Kim, K. Bae, F. B. Prinz and J. H. Shim, *J. Power Sources*, 2020, **465**, 228254.
- 24 S. Molin, A. Chrzan, J. Karczewski, D. Szymczewska and P. Jasinski, *Electrochim. Acta*, 2016, **204**, 136–145.
- 25 H. J. Kim, M. Kim, K. C. Neoh, G. D. Han, K. Bae, J. M. Shin, G. T. Kim and J. H. Shim, *J. Power Sources*, 2016, **327**, 401–407.
- 26 T. Van Gestel, D. Sebold, H. P. Buchkremer and D. Stover, *J. Eur. Ceram. Soc.*, 2012, **32**, 9–26.
- 27 S. Vieweger, R. Mucke, N. H. Menzler and H. P. Buchkremer, *Fuel Cells*, 2013, **13**, 556–564.
- 28 P. Plonczak, M. Joost, J. Hjelm, M. Sogaard, M. Lundberg and P. V. Hendriksen, *J. Power Sources*, 2011, **196**, 1156–1162.
- 29 S. Hwang, J. Lee, G. Kang, M. Choi, S. J. Kim, W. Lee and D. Byun, *J. Mater. Chem. A*, 2021, **9**, 11683–11690.
- 30 I. Jang, S. Kim, C. Kim, H. Lee, H. Yoon, T. Song and U. Paik, *J. Power Sources*, 2019, **435**, 226776.
- 31 A. Tsoga, A. Naoumidis, W. Jungen and D. Stover, *J. Eur. Ceram. Soc.*, 1999, **19**, 907–912.
- 32 L. A. Chick, L. R. Pederson, G. D. Maupin, J. L. Bates, L. E. Thomas and G. J. Exarhos, *Mater. Lett.*, 1990, **10**, 6–12.
- 33 P. Datta, P. Majewski and F. Aldinger, *Mater. Charact.*, 2009, **60**, 138–143.



- 34 C. S. Ding, H. F. Lin, K. Sato and T. Hashida, *Scr. Mater.*, 2009, **60**, 254–256.
- 35 Z. Liu, M. F. Han and W. T. Miao, *J. Power Sources*, 2007, **173**, 837–841.
- 36 A. Ahuja, M. Gautam, A. Sinha, J. Sharma, P. K. Patro and A. Venkatasubramanian, *Bull. Mater. Sci.*, 2020, **43**, 129.
- 37 K. Lee, J. Kang, S. Jin, S. Lee and J. Bae, *Int. J. Hydrogen Energy*, 2017, **42**, 6220–6230.
- 38 N. T. Yang, X. Y. Tan, X. X. Meng, Y. M. Yin and Z. F. Ma, *ECS Trans.*, 2009, **25**, 881–888.
- 39 H. L. Xie and P. C. Su, *Thin Solid Films*, 2015, **584**, 116–119.

